Deterministic drift instability and stochastic thermal perturbations of magnetic dissipative droplet solitons

P. Wills,[1] E. Iacocca,[1,2] and M. A. Hoefer[1]

[1]*Department of Applied Mathematics, University of Colorado, Boulder, Colorado 80302, USA*
[2]*Department of Physics, Division for Theoretical Physics, Chalmers University of Technology, 412 96, Gothenburg, Sweden*
(Received 31 December 2015; published 7 April 2016)

The magnetic dissipative droplet is a strongly nonlinear wave structure that can be stabilized in a thin film ferromagnet exhibiting perpendicular magnetic anisotropy by use of spin transfer torque. These structures have been observed experimentally at room temperature, showcasing their robustness against noise. Here, we quantify the effects of thermal noise by deriving stochastic equations of motion for a droplet based on soliton perturbation theory. First, it is found that deterministic droplets are linearly unstable at large bias currents, subject to a drift instability. When the droplet is linearly stable, our framework allows us to analytically compute the droplet's generation linewidth and center variance. Additionally, we study the influence of nonlocal and Oersted fields with micromagnetic simulations, providing insight into their effect on the generation linewidth. These results motivate detailed experiments on the current and temperature-dependent linewidth as well as drift instability statistics of droplets, which are important figures-of-merit in the prospect of droplet-based applications.

I. INTRODUCTION

Localized magnetic textures have recently attracted significant research interest due to their potential application in logic, storage, and communication technologies. From the perspective of logic and storage, static skyrmions [1] are very interesting textures due to their topological protection against perturbations, small sizes, and controllable motion [2,3]. On the other hand, communication applications could benefit from dynamical textures, notably topological, dynamical skyrmions [4] and nontopological, magnetic dissipative droplets [5–9].

Magnetic dissipative droplets ("droplets" hereafter) have been widely observed in experiments both at cryogenic [10] and room temperatures [11–13]. Droplets exist in magnetic thin films composed of materials with perpendicular magnetic anisotropy (PMA) [14], i.e., in which the easy axis lies normal to the plane, so that it balances the exchange energy in favor of a localized structure [5,15], Fig. 1(a). Furthermore, magnetic damping must also be balanced in order to sustain the droplet in time due to its lack of topology. To date, this has been achieved by using spin transfer torque (STT) [16,17] in devices known as nanocontact spin torque oscillators, NC-STOs [18]. NC-STOs are composed of a pseudo spin valve where two magnetic layers are decoupled by a nonmagnetic spacer, as shown in the schematic of Fig. 1(b). The topmost magnetic layer $\mathbf{m}$ is where the droplet nucleates, and it is usually referred to as the free layer. The bottom magnetic layer $\mathbf{m}_p$ serves as a spin polarizer, and it is known as the polarizer or fixed layer. In order to achieve sufficient current density to oppose magnetic damping, a nanocontact (NC) of radius R_* is placed on top of the free layer, confining the current to flow in an approximately cylindrical path [19] and therefore defining a region of effectively zero damping in the free layer. An external, perpendicular applied field H_0 is generally used in NC-STOs both to tilt the polarizer (useful for increasing STT and magnetoresistance), to provide an external source for the Larmor frequency, and to stabilize the droplet [8].

Since the first experimental observation of droplets [11], recent results have investigated theoretical predictions [5,6,8,20,21], shown the existence of hysteresis both at room and cryogenic temperatures [10,13], and even imaged the droplet via x-ray magnetic circular dichroism (XMCD) [12]. The same studies have demonstrated the existence of characteristics consistent with random droplet dynamics, notably low-frequency spectral features. These have been associated with the droplet exiting the NC region and succumbing to damping, a drift instability, originating from the spatial energy landscape created by the current-induced Oersted field [5,19,22,23] and externally applied fields [8,11,21] or fluctuations in the material anisotropy spatial distribution [13]. However, the relationships between drift instabilities and physical sources of randomness have not been established. To provide an analytical understanding of drift instabilities, we study the effect of thermal noise on droplet dynamics.

In this paper, we develop the stochastic evolution of droplet dynamics based on soliton perturbation theory [21] and obtain statistical observables such as the droplet center variance and the generation linewidth [24]. These results are analytically obtained by linearizing the equations of motion. From the linearization, we uncover a deterministic regime of drift instability, missed by previous analytical works [8,21], where high bias currents induce growth of the droplet velocity on a long timescale. Randomness can also cause an otherwise deterministically stable droplet to be expelled from the NC region when thermal fluctuations are taken into account. We determine that such events are extremely rare relative to the precessional timescale (10–100 picoseconds) but become quite relevant for the typical time scales of experiments (seconds or more). Observation, let alone quantification, of both the deterministic drift instability and the stochastic rare events is practically unfeasible utilizing standard deterministic [5] or stochastic [13] micromagnetic simulations alone. For a stable droplet, the generation linewidth is found to be dominated by the phase noise induced by a Wiener process or random walk, linearly proportional to temperature and
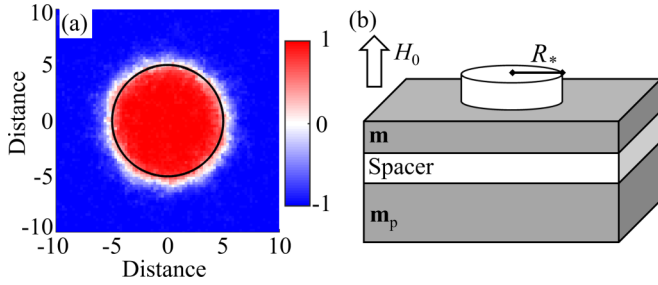
FIG. 1. (a) Typical dissipative droplet obtained from micromagnetic simulations at a finite temperature. The $\hat{\mathbf{z}}$ component of the magnetization is quantified by the color scale. (b) Schematic of a NC-STO based on a pseudo spin valve trilayer. The free, $\mathbf{m}$, and polarizer, $\mathbf{m}_p$, magnetic layers are decoupled by a nonmagnetic spacer. A NC of radius R_* is placed on top of the free layer to achieve high current densities. An external field H_0 is applied perpendicularly to the plane.

inversely proportional to the NC radius. The droplet's center can be described by an Ornstein-Uhlenbeck (O-U) process with STT acting as an attractive mechanism that draws the droplet to the center of the NC. The determination of both stochastic processes requires subtle higher order effects from soliton perturbation theory [8,21]. Full-scale micromagnetic simulations qualitatively agree with the analytical results, even when the current-induced Oersted field is taken into account.

The paper is organized as follows. Section II describes the formalism used to obtain the stochastic equations for droplet dynamics. Section III explores the deterministic linearization where we obtain the fundamental droplet dynamical state and linear stability conditions. Stochastic terms are incorporated into the analysis in Sec. IV, leading to analytical solutions for the droplet center variance and generation linewidth at low temperatures. Numerical simulations of the nonlinear stochastic system are presented in Sec. V, demonstrating excellent agreement with the linearized analytical results. Full-scale micromagnetic simulations are used to explore regimes of small NC radii, nonlocal dipole fields, and Oersted field, beyond the scope of the asymptotic theory, nevertheless demonstrating qualitative agreement. Finally, we provide a discussion and concluding remarks in Sec. VI.

II. DROPLET PERTURBATION THEORY

The analytical study of droplet dynamics can be approached using perturbation theory with the magnetic damping and STT coefficients assumed small. This assumption alone yields droplet nucleation conditions and the resultant droplet's frequency tunability via current and field [5]. A semianalytical generalization can be used to describe coarse droplet motion and control [20]. The additional assumption of a sufficiently large NC diameter implies a slowly precessing, circular domain wall description for the droplet [8], which enables a detailed analytical description of droplet dynamics in the presence of physical perturbation [8,21]. This latter regime is the one considered here.

The equation of motion for the free layer magnetization $\mathbf{m}$ is the Landau-Lifshitz equation for a thin, two-dimensional

magnetic film

$$\frac{\partial \mathbf{m}}{\partial t} = -\mathbf{m} \times \mathbf{h}_{\text{eff}} + \mathbf{p}, \quad \mathbf{m} : \mathbb{R}^2 \times \mathbb{R} \to \mathbb{S}^2, \quad (1)$$

expressed here in nondimensional form. The effective field,

$$\mathbf{h}_{\text{eff}} = h_0 \hat{\mathbf{z}} + \nabla^2 \mathbf{m} + m_z \hat{\mathbf{z}}, \quad (2)$$

includes contributions from a perpendicular external field h_0, the exchange field $\nabla^2 \mathbf{m}$, and a perpendicular magnetic anisotropy (PMA) field sufficient to overcome the thin-film limit of the demagnetizing field. Hence the $m_z \mathbf{z}$ term in the effective field has a positive coefficient, here scaled to unity. This form of the LL equation, with $|\mathbf{m}| = 1$, uses the time scale $\tau = (|\gamma|\mu_0 \eta)^{-1}$, where γ is the gyromagnetic ratio, μ_0 is the vacuum permeability, $\eta = M_s(Q-1)$ is the field scaling, M_s is the free layer's saturation magnetization, $Q = H_k/M_s$ is the nondimensionalized form of the PMA field H_k, and the length scale $L = \lambda_{\text{ex}}/\sqrt{Q-1}$ where λ_{ex} is the exchange length. The NC radius R_* is nondimensionalized to $\rho_* = R_*/L$. We consider a small perturbation $|\mathbf{p}| \ll 1$ satisfying $\mathbf{p} \cdot \mathbf{m} = 0$ in order to preserve constant magnetization magnitude. The perturbation term considered here includes damping, STT as imposed by a NC-STO, and a thermal random field [25]

$$\mathbf{p} = \underbrace{-\alpha \mathbf{m} \times (\mathbf{m} \times \mathbf{h}_{\text{eff}})}_{\text{damping}} + \underbrace{\sigma \mathcal{H}(\mathbf{x}) \mathbf{m} \times \mathbf{m} \times \mathbf{m}_p}_{\text{NC-STO}} - \underbrace{\mathbf{m} \times \mathbf{h}}_{\text{thermal}},$$
(3)

where $0 < \alpha \ll 1$ is the damping parameter,

$$\mathcal{H}(\mathbf{x}) = \begin{cases} 1 & |\mathbf{x}| \leqslant \rho_* \\ 0 & \text{else} \end{cases}$$

is a shifted Heaviside function describing the current path below the NC, $\mathbf{m}_p$ is the normalized polarizer orientation, and $\sigma = I/I_0$ is the nondimensionalized form of the current I, scaled by

$$I_0 = \frac{4\mu_0 M_s^2 (Q-1) e \pi R_*^2 \delta}{\hbar \epsilon}. \quad (4)$$

Here, e is the charge of the electron, δ is the thickness of the free layer, ϵ is the spin torque efficiency, and $\hbar$ is Planck's constant. Example scalings for recent experiments are listed in Table I for reference.

The thermal field $\mathbf{h}(\mathbf{x}, t)$ induces random fluctuations in the magnetization of a small material volume V and is assumed to be delta correlated in space and time, i.e., white noise [25].

TABLE I. Time, length, field, current, and temperature scalings and typical nondimensionalized experimental parameters for recent experiments.

Parameters	Refs. [10] and [12]	Ref. [11]
τ (time, ns)	0.13	0.083
L (length, nm)	13.2	9.25
η (field, kA/m)	198.9	318.1
I_0 (current, mA)	152.75	139.7
T_0 (temperature, kK)	156.0	337.2
σ/α (scaled current to damping)	1.96	6.44
h_0 (scaled applied field)	0.5	2.5
ρ_* (scaled nanocontact radius)	5.96	5.95

The variance of the nondimensional field is $\mathrm{Var}[\mathbf{h}(\mathbf{x},t)] = \beta^2$ with

$$\beta^2 = \frac{T}{T_0}, \quad T_0 = \frac{\mu_0 M_s^2 V}{2\alpha k_B}, \tag{5}$$

where k_B is the Boltzmann constant, $V = \lambda_{\mathrm{ex}}^2 \delta$ is the characteristic micromagnetic volume, and T_0 is the nondimensional scaling of the absolute temperature T. Table I includes typical temperature scalings for recent experiments and our micromagnetic simulations. The perturbative theory utilized here is valid in the low temperature regime where $\beta \ll 1$. The variance in Eq. (5) can be dimensionalized by multiplying (5) by $\tau M_s^2 (Q-1)^2$.

The droplet is characterized by its center position $\boldsymbol{\xi}$, velocity $\mathbf{v}$, collective phase ϕ, and precessional frequency ω. In the regime $0 \leqslant v \ll \omega \ll 1$, where $v = |\mathbf{v}|$ is the droplet speed, the droplet takes on the approximate form of a slowly precessing circular domain wall with a spatial phase proportional to the droplet's speed [21]

$$\cos\Theta = \tanh\left(\rho - \frac{1}{\omega}\right), \tag{6a}$$

$$\Phi = h_0 t - \frac{\mathbf{v}\cdot\hat{\boldsymbol{\rho}}}{\omega^2} + \phi, \quad \phi = \omega t + \phi_0. \tag{6b}$$

Equation (6) describes the magnetization orientation of the droplet in spherical coordinates (Θ, Φ) with polar angle from vertical $0 \leqslant \Theta < \pi$ and azimuthal angle Φ. In Eq. (6), we employ droplet-centered polar coordinates in the plane, so that the radial unit vector $\hat{\boldsymbol{\rho}}$ points from the droplet center $\boldsymbol{\xi}$ to a point in space $\mathbf{x} = (\rho\cos\varphi, \rho\sin\varphi)$ and the angular unit vector $\hat{\boldsymbol{\varphi}}$ is orthogonal $\hat{\boldsymbol{\varphi}}\cdot\hat{\boldsymbol{\rho}} = 0$ and satisfies the right hand rule $\hat{\boldsymbol{\rho}}\times\hat{\boldsymbol{\varphi}} = \hat{\mathbf{z}}$. The structure of the $v = 0$ approximate droplet in Eq. (6) has been known for some time in the absence of STT (see, e.g., Ref. [15]) and the singular $\omega \to 0$ behavior for $v \neq 0$ was identified in Ref. [26].

Following the procedure described in Ref. [21], the slow evolution of the perturbed droplet's parameters for large NC radii $\rho_* \gg 1$, weak damping/STT $\sigma = \mathcal{O}(\alpha) \ll 1$, and low temperature $\beta \ll 1$ is governed by the set of coupled, stochastic differential equations

$$d\phi = \omega\, dt - \frac{\sigma}{4\pi}\int_{|\mathbf{x}|\leqslant\rho_*} (\mathbf{v}\cdot\hat{\boldsymbol{\rho}})\,\mathrm{sech}^2\left(\rho - \frac{1}{\omega}\right)d\mathbf{x}\,dt + d\mathcal{W}_\phi, \tag{7a}$$

$$d\boldsymbol{\xi} = \mathbf{v}\,dt + \frac{\sigma\omega}{2\pi}\int_{|\mathbf{x}|\leqslant\rho_*} \mathrm{sech}^2\left(\rho - \frac{1}{\omega}\right)\hat{\boldsymbol{\rho}}\,d\mathbf{x}\,dt + d\boldsymbol{\mathcal{W}}_{\boldsymbol{\xi}}, \tag{7b}$$

$$d\omega = \alpha\omega^2(\omega + h_0)dt - \frac{\sigma\omega^3}{4\pi}\int_{|\mathbf{x}|\leqslant\rho_*} \mathrm{sech}^2\left(\rho - \frac{1}{\omega}\right)d\mathbf{x}\,dt + d\mathcal{W}_\omega, \tag{7c}$$

$$d\mathbf{v} = \alpha\omega\mathbf{v}(\omega + 2h_0)dt - \frac{\sigma\omega^2}{2\pi}\int_{|\mathbf{x}|\leqslant\rho_*} \left(\frac{3}{2}\mathbf{v} - \frac{(\mathbf{v}\cdot\hat{\boldsymbol{\varphi}})}{\rho\omega}\hat{\boldsymbol{\varphi}}\right)$$
$$\times\,\mathrm{sech}^2\left(\rho - \frac{1}{\omega}\right)d\mathbf{x}\,dt + d\boldsymbol{\mathcal{W}}_{\mathbf{v}}, \tag{7d}$$

which are to be interpreted in the Stratonovich sense [27]. The dynamical system describing modulations of a droplet's

parameters subject to a general class of perturbations was derived in Ref. [21]. The particular form of the stochastic terms in (7) result from the thermal field perturbation $-\mathbf{m}\times\mathbf{h}$ in Eq. (3). The damping (proportional to α) and spin torque (proportional to σ) terms in (7) were also specifically derived in Ref. [21].

There is a symmetry in these equations between the droplet's collective precessional dynamics and motion. The phase ϕ and position $\boldsymbol{\xi}$ dynamics have a leading order linear coupling to the frequency ω and velocity $\mathbf{v}$ equations, respectively. The second, additional terms in the phase and position equations proportional to current σ correspond to higher order corrections from soliton perturbation theory, which prove to be essential for describing perturbed droplet dynamics [8,21], in particular, the finite temperature effects explored here.

The terms $\mathcal{W}_i$, with $i = \phi$, $\boldsymbol{\xi}$, ω, and $\mathbf{v}$, are scaled Weiner processes, with nontrivial covariance structure. Each noise term is a spatial integral of the thermal field perturbation against an appropriate kernel (see Ref. [21], Eqs. 4.1–4.4). If we arrange them into a vector $\boldsymbol{\mathcal{W}} = (\mathcal{W}_\phi\, \mathcal{W}_{\xi_x}\, \mathcal{W}_{\xi_y}\, \mathcal{W}_\omega\, \mathcal{W}_{v_x}\, \mathcal{W}_{v_y})^T$, then the covariance between the processes is given by

$$\mathrm{E}[\boldsymbol{\mathcal{W}}\boldsymbol{\mathcal{W}}^T] = \frac{\beta^2 t}{2\pi}\begin{bmatrix} \sigma_\phi^2 & \mathbf{v}^T/2 & \\ \mathbf{v}/2 & \omega\mathbf{I} & \mathbf{0} \\ & & \omega^5/2 & \omega^4\mathbf{v}^T \\ \mathbf{0} & & \omega^4\mathbf{v} & \sigma_\mathbf{v}^2 \end{bmatrix}, \tag{8}$$

where we have, for the sake of compactness, denoted

$$\sigma_\phi^2 = \frac{v^2}{4\omega} + \frac{\omega}{2}, \tag{9a}$$

$$\sigma_\mathbf{v}^2 = \begin{bmatrix} \omega^5 + \frac{\omega^3}{4}(9v_x^2 + v_y^2) & 2\omega^3 v_x v_y \\ 2\omega^3 v_x v_y & \omega^5 + \frac{\omega^3}{4}(v_x^2 + 9v_y^2) \end{bmatrix}, \tag{9b}$$

and $\mathbf{I}$ is the 2×2 identity matrix and $\mathbf{0}$ is the 3×3 zero matrix.

III. DETERMINISTIC LINEARIZATION AND STABILITY

We will first examine the dynamics of Eqs. (7) at zero temperature $\beta^2 = 0$. These deterministic dynamics have been studied in detail [8,21]. When the current σ exceeds the minimal sustaining current $\sigma_{\min}$, the system undergoes a saddle-node bifurcation resulting in a stable fixed point denoted $(\boldsymbol{\xi}_*, \omega_*, \mathbf{v}_*)$ that encapsulates the balance between damping and STT to sustain the droplet. The stable fixed point is stationary at the center of the NC, $\boldsymbol{\xi}_* = \mathbf{v}_* = 0$, with precessional frequency ω_* determined as a root of the transcendental equation

$$\frac{\sigma}{\alpha} = \frac{2(h_0 + \omega_*)}{1 + \omega_*\left[\log\left(\frac{1}{2}\mathrm{sech}\left(\rho_* - \frac{1}{\omega_*}\right)\right) + \rho_*\tanh\left(\rho_* - \frac{1}{\omega_*}\right)\right]}. \tag{10}$$

We observe that the phase ϕ in Eqs. (7) decouples from the system, so its dynamics can be determined from the remaining three parameters. If we linearize Eqs. (7) around this fixed point, we arrive at the system

$$\dot{\phi} = \omega, \tag{11a}$$

$$\dot{\boldsymbol{\xi}} = \mathbf{v} + \lambda_\xi \boldsymbol{\xi}, \tag{11b}$$

$$\dot{\omega} = \lambda_\omega(\omega - \omega_*), \tag{11c}$$

$$\dot{\mathbf{v}} = \lambda_v \mathbf{v}, \tag{11d}$$

where

$$\lambda_\xi = -\frac{1}{2}\sigma\rho_*\omega_* \text{sech}^2\left(\rho_* - \frac{1}{\omega_*}\right), \tag{12a}$$

$$\lambda_\omega = -h_0\alpha\omega_* + \lambda_\xi + \frac{1}{2}\sigma\omega_*\left(\tanh\left(\rho_* - \frac{1}{\omega_*}\right) + 1\right), \tag{12b}$$

$$\lambda_v = -2\alpha\omega_*^2 + \lambda_\omega - \lambda_\xi. \tag{12c}$$

It is necessary to carefully choose parameters so that this fixed point is stable, i.e., so that all eigenvalues in Eq. (12) are negative. The condition $\sigma > \alpha h_0$ is sufficient for $\lambda_\xi, \lambda_\omega < 0$, but in order to ensure that $\lambda_v < 0$, we require additionally that

$$\alpha\omega_*(2\omega_* + h_0) > \frac{1}{2}\sigma\omega_*\left(\tanh\left(\rho_* - \frac{1}{\omega_*}\right) + 1\right). \tag{13}$$

Note that the inequality requirement for stability in (13) was not identified previously [21], and is essential to understanding the dynamics of the droplet. It is possible to visualize the region of linear stability in the $(h_0, \sigma/\alpha)$ plane as in Fig. 2. The left (red) area corresponds to the condition $\sigma < \sigma_{\min}$, where the droplet cannot exist. This approximately linear relation for the existence boundary has been corroborated by experiment [10]. The inequality requirement Eq. (13) adds an unstable, right region (blue area) where the velocity of the droplet increases until it drifts away from the NC area and damping destroys
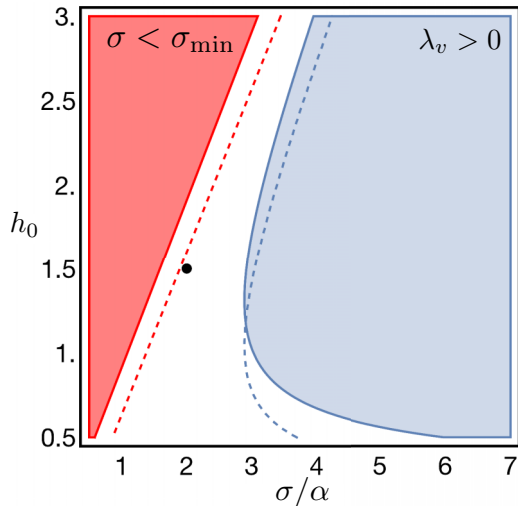

FIG. 2. Droplet existence and linearly stable parameter space for a droplet nucleated in a NC of normalized radius $\rho_* = 15$. The droplet cannot exist in the left region (filled red) where $\sigma < \sigma_{\min}$, whereas the droplet is linearly unstable in the right region (filled blue) where $\lambda_v > 0$. Therefore, the droplet is stable in the remaining white region. The numerical simulations in Sec. V and Figs. 3, 4, and 5(a) with $h_0 = 1.5$, $\alpha = 0.03$, and $\sigma = 2\alpha$ (black circle) exhibit linear stability. The dashed lines are boundaries for droplet existence and linear stability with reduced NC radius $\rho_* = 5$.

it. The remaining white area represents the parameter space where the droplet exists and is stable. We observe that such a region shifts to lower applied fields and increased current for smaller NC radii (dashed lines).

It is helpful to express these eigenvalues in a more tractable form, so that we can observe how they approximately scale with experimental parameters. For this, we define a parameter-dependent constant that we will denote by ζ

$$\zeta = \frac{2\alpha h_0}{\sigma} - 1. \tag{14}$$

Previous work [21] assumed that the current was near the critical value $\sigma \approx 2\alpha h_0$, so that $\zeta = \mathcal{O}(\rho_*^{-1})$. This work relaxes that assumption and allows for any current that is sufficiently above the minimum sustaining current so that Eq. (10) can be approximately inverted to obtain the frequency tunability

$$\omega_* = \rho_*^{-1} + \text{arctanh}(\zeta)\rho_*^{-2} + \mathcal{O}(\rho_*^{-3}). \tag{15}$$

Then the leading-order approximations of each eigenvalue are

$$\lambda_\xi = -\frac{\sigma}{2}(1 - \zeta^2) + \mathcal{O}(\rho_*^{-1}), \tag{16a}$$

$$\lambda_\omega = -\frac{\sigma}{2}(1 - \zeta^2) + \mathcal{O}(\rho_*^{-1}), \tag{16b}$$

$$\lambda_v = \mathcal{O}(\sigma\rho_*^{-2}). \tag{16c}$$

The approximate expression for λ_v is prohibitively complex, so we omit it here in favor of the exact expression in Eq. (12).

Inequality (13) is a fundamental result identifying a deterministic mechanism that can drive droplet drift instability. Any nonzero $\mathbf{v}$ [recall that $\mathbf{v} \neq 0$ corresponds to a spatial phase gradient across the droplet in Eq. (6b)] will slowly increase when Eq. (13) does not hold. Large applied current destabilizes the droplet.

Previous work [8] that analyzed the dynamics of this system with $\mathbf{v} \equiv 0$ found that the dissipative droplet is linearly stable for physically relevant parameters. The sole effect of damping on a stationary droplet's frequency $d\omega/dt = \alpha\omega^3$ has been known for some time [28]. While this result demonstrates that the droplet is unstable in the presence of damping alone, it does not describe the instability investigated here with STT included. Similarly, Ref. [20] observed instability in the case $v \neq 0$ without taking into account STT. Our contribution here is to extend the dynamics to incorporate STT, thereby uncovering current dependent regimes of deterministic instability. In Ref. [21], the dynamics are analyzed, but the linear instability condition (13) was not recognized. The recognition of this linear instability, occurring at physically relevant parameters, is essential to the understanding of droplet dynamics. When $\mathbf{v} \neq 0$, the dynamics are much more sensitive to the choice of parameters, as is seen both above in the linear case and below in the full nonlinear case. A key observation is that while $\lambda_\xi, \lambda_\omega$ are small $\mathcal{O}(\sigma)$, λ_v is much smaller $\mathcal{O}(\sigma\rho_*^{-2})$. These eigenvalues dictate the relaxation rate of the system towards the fixed point.

When compared to the $\mathbf{v} = 0$ dynamics, the relaxation rate of the droplet center $\boldsymbol{\xi}$ decreases by a factor proportional to $\rho_*^{-2} \ll 1$ when the $\mathbf{v}$ dynamics are included. Furthermore, we see that λ_v can change sign, while λ_ξ and λ_ω are negative

for $\sigma > \alpha h_0$. This suggests that there is a shallow basin of attraction for the fixed point, allowing for the possibility of linear drift instabilities mediated by thermal noise. Indeed, all experiments [10–12] have been performed outside the region of linear stability, suggesting droplet drift instability and the concomitant observation of low-frequency spectral features. We note that the theory presented here is nominally applicable to the case $\rho_* \gg 1$, whereas the experiments in Refs. [10–12] with $\rho_* \in (5,8)$ are at the borderline of applicability.

IV. STOCHASTIC LINEARIZATION

One method of approximating the dynamics of the stochastic system Eqs. (7) is to employ the previously calculated linearization of the deterministic system and approximate the noise, now denoted $\mathcal{W}^*$, by evaluating the covariance matrix, Eq. (8), at the fixed point. This low temperature theory yields the linear stochastic system

$$d\phi = \omega dt + d\mathcal{W}_\phi^*, \tag{17a}$$

$$d\boldsymbol{\xi} = \mathbf{v}dt + \lambda_\xi \boldsymbol{\xi} dt + d\mathcal{W}_\xi^*, \tag{17b}$$

$$d\omega = \lambda_\omega(\omega - \omega_*)dt + d\mathcal{W}_\omega^*, \tag{17c}$$

$$d\mathbf{v} = \lambda_v \mathbf{v}dt + d\mathcal{W}_\mathbf{v}^*. \tag{17d}$$

When evaluated at the fixed point, the covariance matrix becomes diagonal

$$\mathrm{E}[\mathcal{W}^* \mathcal{W}^{*T}] = \beta^2 t \cdot \mathrm{Diag}\left(\frac{\omega_*}{4\pi}, \frac{\omega_*}{2\pi}, \frac{\omega_*}{2\pi}, \frac{\omega_*^5}{4\pi}, \frac{\omega_*^5}{2\pi}, \frac{\omega_*^5}{2\pi}\right),$$

$$\equiv t \cdot \mathrm{Diag}\left(\beta_\phi^2, \beta_\xi^2, \beta_\xi^2, \beta_\omega^2, \beta_v^2, \beta_v^2\right), \tag{18}$$

where we denote the variance of each parameter by β_i^2 for $i = \phi, \boldsymbol{\xi}, \omega$, and $\mathbf{v}$. The linear system Eqs. (17) can be solved explicitly. For $(\boldsymbol{\xi}, \omega, \mathbf{v})$, we obtain a set of coupled O-U processes that describe the stochastic properties of the linear system.

Of particular interest is the behavior of the decoupled oscillator phase, $\phi(t)$, as it allows us to relate our analytical description with the generation linewidth, Δf, which can be measured from the electrical characterization of NC-STOs [18]. Solving the system in Eqs. (17), we find that the frequency is an O-U process with mean ω_* and variance

$$\mathrm{Var}[\omega(t)] = -\frac{\beta_\omega^2}{2\lambda_\omega}(1 - \exp 2\lambda_\omega t)$$

$$\rightarrow -\frac{\beta_\omega^2}{2\lambda_\omega}, \quad \text{as } t \rightarrow \infty. \tag{19}$$

We can then write down the solution for the phase $\phi(t)$ as the sum of an integrated O-U process and a Wiener process (random walk)

$$\phi(t) = \int_0^t \omega(s)ds + \mathcal{W}_\phi^*, \tag{20}$$

from which we find that the variance of ϕ quickly approaches linear growth

$$\mathrm{Var}[\phi(t)] \rightarrow \left(\frac{\beta_\omega^2}{\lambda_\omega^2} + \beta_\phi^2\right)t \quad \text{as } t \rightarrow \infty, \tag{21}$$

so that the spectral line shape is Lorentzian and the generation linewidth is given by

$$\Delta f = \left(\frac{\beta_\omega^2}{\lambda_\omega^2} + \beta_\phi^2\right) = \beta^2\left(\frac{\omega_*^5}{4\pi\lambda_\omega^2} + \frac{\omega_*}{2\pi}\right). \tag{22}$$

By virtue of Eq. (5), the generation linewidth is linearly proportional to temperature. Because $\omega_* \ll 1$, the generation linewidth is dominated by the Wiener process, phase noise contribution [second term in Eq. (22)] resulting from the higher order contribution to the phase dynamics of Eq. (7a). This expression for generation linewidth is also consistent with the notion of a reduced impact of thermal fluctuations on a larger magnetic mode volume. Indeed, recalling Eq. (15), it is clear that larger NC radii minimize the generation linewidth.

We are also interested in the dynamics of the center $\boldsymbol{\xi}$ as it describes the droplet's random motion with respect to the NC region. The velocity and position form a coupled pair of O-U processes, which we can solve using standard methods. We then find the variance of the droplet center

$$s_\xi^2(t) = -\frac{\beta_\xi^2}{2\lambda_\xi}(1 - e^{2\lambda_\xi t}) - \frac{\beta_v^2}{2(\lambda_\xi - \lambda_v)^2}$$

$$\times \left(\frac{1 - e^{2\lambda_\xi t}}{\lambda_\xi} + \frac{4(1 - e^{(\lambda_\xi + \lambda_v)t})}{\lambda_\xi + \lambda_v} + \frac{1 - e^{2\lambda_v t}}{\lambda_v}\right)$$

$$\rightarrow -\frac{1}{2}\frac{\beta_v^2}{\lambda_\xi^2\lambda_v} - \frac{\beta_\xi^2}{\lambda_\xi} \quad \text{as } t \rightarrow \infty. \tag{23}$$

We might expect that the position noise term in Eq. (23) would dominate, analogous to the phase noise in Eq. (22). However, the balance of the two terms in Eq. (23) is highly sensitive to experimental parameters. In fact, for the parameters used in this study, the velocity noise term is the dominant contribution.

Equations (22) and (23) are central results of this paper. The former relates our stochastic theory to an experimental observable, namely, the Lorentzian generation linewidth. The latter quantifies the amount of droplet drift with respect to the NC center and thus provides a means to quantify the drift instability from random fluctuations in the magnetic system.

V. NUMERICAL SIMULATIONS

To examine the behavior of the full nonlinear system, Eqs. (7), we numerically simulate an ensemble of sample paths. Details of our numerical implementation can be found in the Appendix. We choose the parameters $\rho_* = 15$, $h_0 = 1.5$, $\alpha = 0.03$, and $\sigma = 2\alpha$ in order to ensure that we are within the asymptotic validity of our analysis and the region of linear stability, depicted by the black dot in Fig. 2. Typical sample paths of the droplet's phase and center position generated by this method are shown in Fig. 3.

We first examine the statistics of the droplet center. Figure 4 shows the standard deviation of the droplet center for an ensemble of numerical simulations of the linear (blue) and nonlinear (red) systems. The analytical prediction of Eq. (23) (black) agrees well with the linear simulation. For the chosen set of parameters, nonlinearity is not observed to significantly enhance the droplet drift and, in fact, the standard deviation of the droplet center from the NC center is never more than 1% of the NC radius. For slightly modified parameters, we
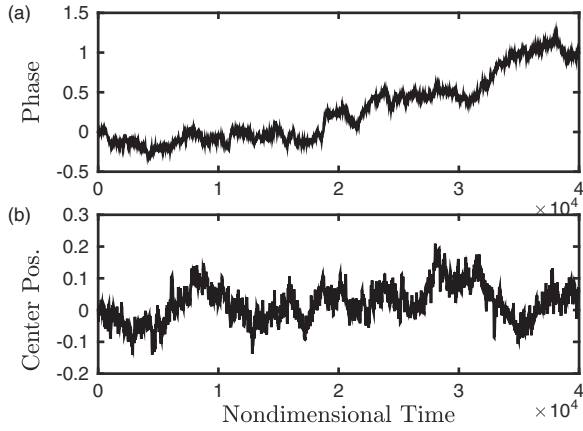
FIG. 3. Numerically computed nonlinear sample path from Eqs. (7) for (a) the droplet phase ϕ and (b) the x component of the center position ξ_x. The phase is measured in radians, and position and time are nondimensional as per Table I.

observe qualitatively different behavior when nonlinearity is introduced. For example, reducing the NC radius to $\rho_* = 10$, we approach the stability boundary of Fig. 2, although linear stability in Eq. (13) is still satisfied. However, the numerical simulation of the nonlinear system leads to approximately 15% of the simulated paths leaving the NC before $t = 4 \times 10^4$. This indicates that the basin of attraction of the system is relatively small. We can also infer from the simulations at larger NC radii that the size of the basin of attraction decreases with NC radius. This suggests that the small NC devices used in experiments at room temperature sustain droplets that exhibit deterministic or thermally induced drift instabilities during measurements. In fact, typical spectral measurements [11,13] acquire data in time spans on the order of seconds, which translate to $\approx 1 \times 10^{10}$ in our normalized units. The characterization of the multidimensional boundary in phase space of the basin of attraction and ejection statistics are, however, outside the scope of this paper. Note that in the ensemble used to generate Fig. 4, no sample paths ejected from the NC.
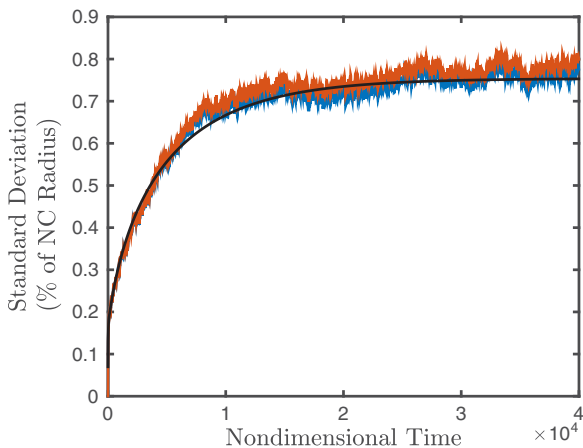

FIG. 4. Standard deviation s_ξ of the droplet center from linear theory (solid black line), linear simulation (solid blue), and nonlinear simulation (solid red).
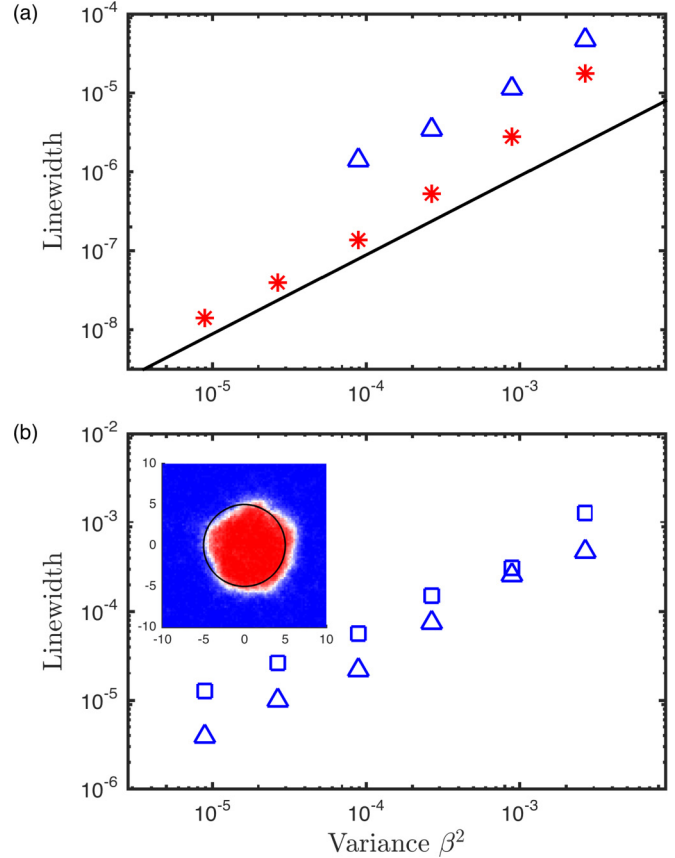

FIG. 5. (a) Droplet linewidth as a function of temperature from linear theory (solid black line), nonlinear simulation (red asterisks), and micromagnetic simulations (blue triangles) when $\rho_* = 15$, $h_0 = 1.5$, $\alpha = 0.03$, $\sigma = 2\alpha$. (b) Droplet linewidth as a function of temperature from micromagnetic simulations where only the NC radius is reduced to $\rho_* = 5$ from (a) (blue triangles) and the effect of a current-induced Oersted field (blue squares). Linewidth is expressed in rad/τ as per Table I. Inset shows droplet profile with Oersted field included. Error bars are $\mathcal{O}(10^{-9})$ and are not shown.

In the regime where the droplet does not drift away from the NC over the timescale simulated, it is possible to compare the linear generation linewidth to numerical simulations of Eqs. (7). From a sample path of the stochastic phase $\phi(t)$, we calculate the linewidth via the power spectral density of ϕ, as discussed in Ref. [24]. It is worth noting that the linewidth calculated via this method is strictly valid for white noise [29] and can vary between sample paths due to the fluctuations between each path. For the linewidths reported here, we take the mean value of the calculated linewidths from 500 different sample paths. Figure 5(a) shows the linewidth's dependence on temperature for the nonlinear system (red asterisks) and Eq. (22) (solid black line). Finite sampling and the asymmetric, heavy-tailed distribution of linewidths across sample paths causes the mean to converge slowly to the linear theory at low temperature. Although the median gives results more clearly convergent to the linear theory, the mean corresponds to experimentally observed linewidths, which are averaged over long timescales. Nonlinear simulations yield a mean linewidth of 1.77×10^{-5} at temperature $\beta^2 = 2.8 \times 10^{-3}$, which, for

comparative purposes, corresponds to 214 kHz at temperature $T = 314$ K under the temporal and temperature scalings of Ref. [11] with damping enhanced to $\alpha = 0.03$. Note, however, that the material parameters (ρ_*, σ, and h_0) for the nonlinear simulations do not correspond to those from Ref. [11].

The linear theory is a very good predictor of the nonlinear system's behavior at low temperatures, and we numerically observe that the discrepancy between the linear and nonlinear linewidths decreases quadratically in T as $T \to 0$, as one would expect from this perturbative approach. However, as room temperature is approached, the nonlinear linewidth exceeds the linear linewidth by an order of magnitude. This originates from the increased impact of thermal fluctuations when the linearization is not strictly applicable. We stress that current experiments have not directly detected ejection events, and in the event of ejection, the bias current can renucleate a droplet, and the resulting linewidth in aggregate will be considerably broader due to the ensuing transient dynamics. Our simulations end upon ejection, and do not allow for renucleation.

The above simulations are strictly valid for the regime $\rho_* \gg 1$ with negligible long-range dipole and Oersted fields. Experiments to date, however, have been performed when $\rho_* \in (5,8)$. Moreover, it is important to characterize the impact of dipolar and Oersted fields on the droplet's collective motion and precession. To further explore droplet behavior, we perform full-scale micromagnetic simulations with nonlocal dipole fields using the GPU-based package Mumax3 [30]. We first compare micromagnetic results by choosing the same set of dimensionless parameters specified above and scalings consistent with Co/Ni multilayers [11] (See Table I). The fixed layer is assumed to be perpendicularly polarized. The NC is placed at the geometrical center of an active area of size $89.9 \times 89.9 \times 0.39$ discretized in cells with size $0.35 \times 0.35 \times 0.39$, below the exchange length. An ensemble of sample paths is not feasible to compute micromagnetically due to time constraints, so we determine the linewidth from a single path spanning $t = 1.8 \times 10^4$ and sampled at 0.015 intervals. First, we do not observe droplet motion, which is consistent with the results shown in Fig. 4 where the droplet center variance is expected to be below our cell resolution. The results for the temperature dependent linewidth are shown in Fig. 5(a) as blue triangles. We note that the micromagnetic simulations overestimate the linewidth obtained from nonlinear simulations but are on the same order of magnitude at room temperatures. At low temperatures, the micromagnetic simulations do not approach the linear theory as one would expect. This is a consequence of the limited simulation time and the spatial resolution of our micromagnetic scheme that precludes an accurate estimation of the phase noise statistics and thus its convergence to the linear linewidth.

Despite this limitation, micromagnetic simulations can be used to explore the dynamics of droplets sustained in devices with smaller NC radii, where micromagnetics have shown to be more accurate [11,13] and where, conversely, the theory is not strictly applicable. We perform micromagnetic simulations with the same nondimensional parameters specified above but reduce the NC radius to $\rho_* = 5$, in the range of experiments performed to date, and increase the current to $\sigma = 0.1$. The resulting linewidths are shown in Fig. 5(b) by blue triangles. A qualitative agreement with theory is observed, namely, a linear dependence of the linewidth on temperature and a linewidth

increase for smaller NC radii. Additionally, micromagnetic simulations allow us to include the current-generated Oersted field [19,22,23]. This further enhances the linewidth by a factor ~ 5 (blue squares) originating from the distortion of the droplet boundary, as observed from a snapshot of the $\hat{\mathbf{z}}$ magnetization component shown in the inset of Fig. 5(b). These results suggest that the unavoidable nonlocal and Oersted fields in a real device will enhance the generation linewidth compared to theory, but the temperature-dependent features remain mostly unchanged.

VI. DISCUSSION AND CONCLUSION

We have developed a stochastic perturbation theory for magnetic dissipative droplets describing the random motion of the droplet's position, velocity, frequency, and phase. Higher-order perturbative effects in the phase and position are shown to be essential for understanding the dynamics of the droplet. Inclusion of velocity dynamics causes a qualitative shift in the behavior of the droplet position and gives rise to a previously uncovered deterministic drift instability. Such an instability occurs at high driving currents, leading to an exponential increase in the droplet velocity. This effect also implies a small basin of attraction for the stable fixed point, providing a simple explanation for the origin of drift instabilities from randomness in the system, such as thermal fluctuations.

We find that in parameter regimes where the deterministic droplet is linearly stable, the stochastically induced drift instabilities are rare events compared with the typical precessional timescales. A notable implication is that the observation of drift instabilities due to thermal fluctuations using micromagnetic simulations is prohibitive. In contrast, our finite dimensional reduction of the governing partial differential equation makes such effects computationally feasible. The study of rare events is beyond the scope of this paper, but motivates an application of large deviation theory, as previously studied, for example, in the context of fiber optic soliton communication systems [31]. Likewise, micromagnetic simulations tailored to study rare events [32] might be used to resolve the time and computational limitations. Even in the deterministic case, the predicted linear instability may be difficult to recover from micromagnetic simulations due its slow rate of exponential growth. From an experimental point of view, typical measurement timescales suggest that drift instability and droplet renucleation can occur many times. For example, the long timescale required in the direct imaging of localized excitations, 500 ms, indicates that drift instabilities could occur $\sim 10^6$ times, leading to the small droplet amplitude and spatial smearing observed in the XMCD images of Ref. [12].

In contrast, previous works have interpreted the droplet drift mechanism through spatial inhomogeneities in field [21] or anisotropy [13]. Here, we have identified two additional drift mechanisms, a deterministic linear instability inherent to the NC-STO system and rare drift events caused by thermal fluctuations.

Our model also allows us to obtain an analytical expression for the linearly stable droplet generation linewidth. At low temperature, we find that the phase noise is characterized by a Wiener process (random walk) and the droplet center is an O-U process, analogous to the stochastic phase and am-

plitude dynamics, respectively, of spatially uniform STOs [24]. For the linearized system, the resulting generation linewidth is linearly dependent on temperature, whereas the nonlinear system exhibits a linewidth enhancement when approaching room temperature, reflecting the coupling between the droplet's constituent variables. Full-scale micromagnetic simulation, including the fully nonlinear spatial variation of the system, qualitatively agree with the numerical results. However, we do not observe convergence toward the linear theory at low temperatures using a standard micromagnetic package [30]. This suggests the study of droplet generation linewidth as a test problem for stochastic micromagnetic codes [33].

The analytical and numerical linewidths obtained are two orders of magnitude below the typical linewidths observed in experiments. This disagreement may be caused by the small NC radii used experimentally, the existence of nonlocal dipolar and current-induced Oersted fields, and the aforementioned drift instabilities for data-acquisition timescales. In fact, micromagnetic simulations performed with a radius similar to those experimentally fabricated to date return linewidths in the same order of magnitude when both nonlocal and current-induced Oersted fields are included. The relevance of such fields in the generation linewidth motivates their inclusion in the analytical theory. For thin films, the effect of nonlocal dipole fields on deterministic droplet dynamics has been shown to be a frequency downshift when $\mathbf{v} = 0$ [8]. It remains to incorporate these effects into the stochastic theory when $\mathbf{v} \neq 0$. Because the Oersted field is not a singular perturbation [21], its inclusion in this collective theory would necessitate the incorporation of droplet coupling to spin waves. Such coupling is in principle possible, see, e.g., Ref. [34].

In conclusion, this paper provides the means to seek optimized experimental parameters for a given application. To wit, we find that an environment with a large NC radius, low field, modest current, and large anisotropy is less susceptible to drift and thus leads to a much narrower generation linewidth. Our results motivate a more detailed experimental study on the current and temperature-dependent generation linewidth and ejection statistics of droplets.
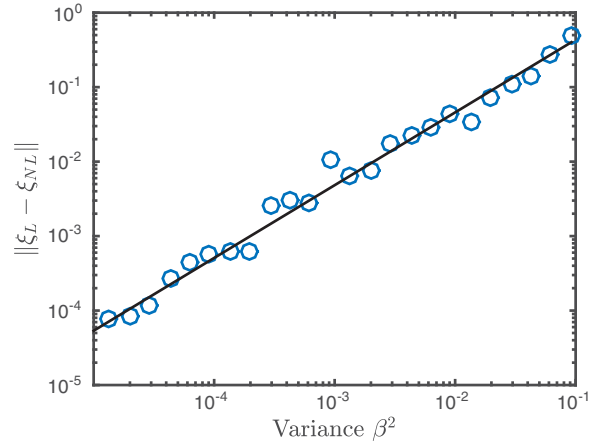
FIG. 6. Convergence plot indicating that $|\xi_{\mathrm{NL}} - \xi_{\mathrm{L}}| = \mathcal{O}(\beta^2) = \mathcal{O}(T)$. Best-fit line has slope of 0.9793.

APPENDIX: NUMERICAL METHODS

We simulate the nonlinear system Eq. (7) via the Euler-Maruyama method, with drift correction to account for the Stratonovich interpretation of the stochastic integrals [35]. Results of the higher-order Milstein scheme [35] yield negligibly different results. For example, the linewidth at room temperature differed by < 1% between the Euler and Milstein simulations. We use a time step of $dt = 4$, and our total integration time is $t = 4 \times 10^4$. We integrate 500 sample paths, and then use the standard sample variance to produce Fig. 4.

We must ensure that our nonlinear and linear systems coincide when $T \to 0$. To that end, we calculate the pathwise difference between the droplet center $\boldsymbol{\xi}_{\mathrm{L}}$ calculated by discretizing the linear system Eq. (17) and the droplet center $\boldsymbol{\xi}_{\mathrm{NL}}$ calculated via discretizing the nonlinear system Eq. (7). Note that both paths are calculated using the same stochastic terms, scaled appropriately. The results are shown in Fig. 6. The standard deviation of the droplet center from the fixed point is $\mathcal{O}(\sqrt{T})$, and the separation between the nonlinear and linear paths is $\mathcal{O}(T)$, so we have

$$\|\boldsymbol{\xi}_{\mathrm{NL}}(t) - \boldsymbol{\xi}_{\mathrm{L}}(t)\| = \mathcal{O}(s_{\tilde{\xi}}^2). \tag{A1}$$

This linear convergence in T is a positive consistency check on the linearization Eq. (17) and stochastic time stepping of the nonlinear system Eq. (7).

[1] N. Nagaosa and Y. Tokura, Nat. Nano. **8**, 899 (2013).

[2] N. Romming, C. Hanneken, M. Menzel, J. E. Bickel, B. Wolter, K. von Bergmann, A. Kubetzka, and R. Wiesendanger, Science **341**, 636 (2013).

[3] J. Sampaio, V. Cros, S. Rohart, A. Thiaville, and A. Fert, Nat. Nano. **8**, 839 (2013).

[4] Y. Zhou, E. Iacocca, A. Awad, R. K. Dumas, H. Zhang, H. B. Braun, and J. Åkerman, Nat. Comm. **6**, 8193 (2015).

[5] M. A. Hoefer, T. J. Silva, and M. W. Keller, Phys. Rev. B **82**, 054432 (2010).

[6] M. A. Hoefer and M. Sommacal, Physica D **241**, 890 (2012).

[7] M. D. Maiden, L. D. Bookman, and M. A. Hoefer, Phys. Rev. B **89**, 180409 (2014).

[8] L. D. Bookman and M. A. Hoefer, Phys. Rev. B **88**, 184401 (2013).

[9] E. Iacocca, R. K. Dumas, L. Bookman, M. Mohseni, S. Chung, M. A. Hoefer, and J. Åkerman, Phys. Rev. Lett. **112**, 047201 (2014).

[10] F. Macià, D. Backes, and A. Kent, Nat. Nano. **10**, 1038 (2014).

[11] S. M. Mohseni, S. R. Sani, J. Persson, T. N. A. Nguyen, S. Chung, Y. Pogoryelov, P. K. Muduli, E. Iacocca, A. Eklund, R. K. Dumas, S. Bonetti, A. Deac, M. A. Hoefer, and J. Åkerman, Science **339**, 1295 (2013).

[12] D. Backes, F. Macià, S. Bonetti, R. Kukreja, H. Ohldag, and A. D. Kent, Phys. Rev. Lett. **115**, 127205 (2015).

[13] S. Lendínez, N. Statuto, D. Backes, A. Kent, and F. Macià, Phys. Rev. B **92**, 174426 (2015).

[14] P. Bruno and J. P. Renard, Appl. Phys. A **49**, 499 (1989).

[15] A. Kosevich, B. Ivanov, and A. Kovalev, Phys. Rep. **194**, 117 (1990).

[16] L. Berger, Phys. Rev. B **54**, 9353 (1996).

[17] J. C. Slonczewski, J. Magn. Magn. Mater. **159**, L1 (1996).

[18] R. K. Dumas, S. R. Sani, S. M. Mohseni, E. Iacocca, Y. Pogoryelov, P. K. Muduli, S. Chung, P. Dürrenfeld, and J. Åkerman, IEEE Trans. Mag. **50**, 4100107 (2014).

[19] S. Petit-Watelot, R. M. Otxoa, and M. Manfrini, Appl. Phys. Lett. **100**, 083507 (2012).

[20] M. A. Hoefer, M. Sommacal, and T. J. Silva, Phys. Rev. B **85**, 214433 (2012).

[21] L. D. Bookman and M. A. Hoefer, Proc. Roy. Soc. A **471**, 2197 (2015).

[22] R. K. Dumas, E. Iacocca, S. Bonetti, S. R. Sani, S. M. Mohseni, A. Eklund, J. Persson, O. Heinonen, and J. Åkerman, Phys. Rev. Lett. **110**, 257202 (2013).

[23] M. Madami, E. Iacocca, S. Sani, G. Gubbiotti, S. Tacchi, R. K. Dumas, J. Åkerman, and G. Carlotti, Phys. Rev. B **92**, 024403 (2015).

[24] T. Silva and M. Keller, IEEE Trans. Mag. **46**, 3555 (2010).

[25] W. F. Brown, Phys. Rev. **130**, 1677 (1963).

[26] B. Ivanov and V. Stephanovich, Phys. Lett. A **141**, 89 (1989).

[27] M. d'Aquino, C. Serpico, G. Coppola, I. D. Mayergoyz, and G. Bertotti, J. Appl. Phys. **99**, 08B905 (2006).

[28] V. G. Baryakhtar, B. A. Ivanov, A. L. Sukstanskii, and E. Y. Melikhov, Phys. Rev. B **56**, 619 (1997).

[29] A. Eklund, S. Bonetti, S. R. Sani, S. Majid Mohseni, J. Persson, S. Chung, S. A. H. Banuazizi, E. Iacocca, M. Östling, J. Åkerman, and B. Gunnar Malm, Appl. Phys. Lett. **104**, 092405 (2014).

[30] A. Vansteenkiste, J. Leliaert, M. Dvornik, M. Helsen, F. Garcia-Sanchez, and B. Van Waeyenberge, AIP Adv. **4**, 107133 (2014).

[31] R. O. Moore, G. Biondini, and W. L. Kath, SIAM Rev. **50**, 523 (2008).

[32] C. Vogler, F. Bruckner, B. Bergmair, T. Huber, D. Suess, and C. Dellago, Phys. Rev. B **88**, 134409 (2013).

[33] C. Ragusa, M. d'Aquino, C. Serpico, B. Xie, M. Repetto, G. Bertotti, and D. Ansalone, IEEE Trans. Mag. **45**, 3919 (2009).

[34] W. L. Kath and N. F. Smyth, Phys. Rev. E **51**, 1484 (1995).

[35] P. E. Kloeden and E. Platen, *Numerical solution of Stochastic Differential Equations* (Springer-Verlag, Berlin Heidelberg, 1992).